

# Single photoelectron charge spectra of MCP-PMTs coated by Atomic Layer Deposition

Jun Weng<sup>a,b,c</sup>, Aiqiang Zhang<sup>a,b,c</sup>, Qi Wu<sup>d</sup>, Lishuang Ma<sup>d</sup>, Sen Qian<sup>d</sup>, Benda Xu<sup>a,b,c,\*</sup>, Zhe Wang<sup>a,b,c</sup>, Shaomin Chen<sup>a,b,c</sup>

<sup>a</sup>*Department of Engineering Physics, Tsinghua University, Beijing, 100084, China*

<sup>b</sup>*Center for High Energy Physics, Tsinghua University, Beijing, 100084, China*

<sup>c</sup>*Key Laboratory of Particle & Radiation Imaging (Tsinghua University), Ministry of Education, China*

<sup>d</sup>*Institute of High Energy Physics, Chinese Academy of Sciences, Beijing, 100049, China*

---

## Abstract

The atomic layer deposition (ALD) coating lengthens the lifetimes of microchannel plates (MCP), allowing them to act as the electron amplifier of photomultiplier tubes (PMT). At the Jinping Neutrino Experiment (JNE), the single electron response (SER) charge distribution of the newly developed 8-inch MCP-PMT with ALD coating exhibits departures from the Gaussian distribution in large charge regions. To understand and model the mechanism of the large-charged SER, we design a voltage-division experiment to quantify the response of the MCP gains to the different energies of incident electrons. Combining with the Furman probabilistic model, this work first studies secondary electron emission (SEE) in pulse mode and reproduces the SER charge spectra by introducing an additional MCP-surface amplification mode. Our results favor a Gamma-Tweedie mixture to describe the SER charge spectra of MCP-PMTs based on it.

---

**Keywords:** MCP-PMT, single electron response, secondary electron emission, Gamma distribution, Tweedie distribution

## 1. Introduction

PMTs are vital devices in neutrino detection, consisting of a photocathode, an electron multiplier, and an anode [4]. Photons from a light source incident on the photocathode follow a Poisson process. Some photons are converted to electrons via photoelectric effect and the electrons are collected by the multiplier [8], which are Bernoulli selections with the probabilities being Quantum

---

\*Corresponding author

Email address: orv@tsinghua.edu.cn (Benda Xu)

Efficiency (QE) and Collection Efficiency (CE). The photoelectrons (PEs,  $n_{\text{PE}}$ ) count in a specific time interval follows a Poisson distribution [3].

The electron amplification at the multiplier is based on the SEE [32] that when an incident particle, electron or ion, collides with or goes through a solid surface, one or more secondary electrons are emitted from the surface [6]. The average number of secondary electrons produced per incident particle is secondary-emission yield (SEY,  $\delta$ ), and the energy distribution of the secondary electrons (SES) is related to the initial energy of incident particle, incident angle, target material, etc. [10]. Bruining [5], Ushio [31], and Jokela [13] conducted target-shooting experiments using electron guns, and measured the SEY in current mode. L. Olano measured the SES of Kapton, Teflon and Ultem by charging analysis and found the energies are much smaller than that of the primary electrons [27]. Such results are then extrapolated to PMTs [22, 12]. Nevertheless, the low light intensity at which a PMT operates makes the incident electrons discrete. Therefore, one should be more careful when extending the SEY from current mode to a single electron case which is pulse mode.

After amplification by the multiplier, one electron produces over  $10^6$  electrons collected at the anode almost simultaneously. The energies of photoelectrons when produced at the photocathode is only a few eV [24], the initial energies of them are almost determined by the voltage difference between the photocathode and the multiplier, therefore the gains for them are the same. The output charge is often described by a Gaussian distribution in light of the central limit theorem of probability [3]. The probability density function (PDF) for the total charge  $Q$  of several PEs is,

$$\begin{aligned} f(Q) &= P_{\pi}(n_{\text{PE}}; \lambda) \bigotimes f_{\mathcal{N}}(Q; n_{\text{PE}}Q_1, n_{\text{PE}}\sigma_1^2) \\ &= \sum_{n_{\text{PE}}=0}^{\infty} \frac{\lambda^{n_{\text{PE}}} e^{-\lambda}}{n_{\text{PE}}!} \frac{1}{\sigma_1 \sqrt{2\pi n_{\text{PE}}}} \exp \left[ -\frac{(Q - n_{\text{PE}}Q_1)^2}{2n_{\text{PE}}\sigma_1^2} \right] \end{aligned} \quad (1)$$

where  $\lambda$  is the average number of photoelectrons collected by the multiplier,  $Q_1$  is the mean charge of a photoelectron, and  $\sigma_1$  is its standard deviation.  $P_{\pi}(n_{\text{PE}}; \lambda)$  and  $f_{\mathcal{N}}$  are the PDFs of the Poisson distribution and Gaussian. When  $\lambda$  is less than 0.1, the probability of two or more photoelectrons observed is less than one-tenth of the probability of one photoelectron. The two visible peaks are attributed to the pedestal ( $Q = 0$ ) and the single photoelectron ( $Q = Q_1$ ) [33] as blue histogram shown in Fig 1. We study the SER charge spectrum divided by  $Q_1$  as  $Q/Q_1$  to align the gains of different PMTs.

Compared to a large-sized dynode-chain commonly used in PMT, MCP-PMTs employ MCPs

with the high gain and time resolution as electron multipliers [32], and are currently in use or planned for particle physics experiments, such as neutrino experiments like Jiangmen Underground Neutrino Observatory (JUNO) [38] and JNE [36], collider experiments like Belle II TOP detector [23] and PANDA DIRC Cherenkov detector at FAIR [18], and cosmic ray observation experiments like LHAASO [7]. Initially, MCP-PMTs were limited by lifetime issues caused by the damage of MCP film layers [17]. A precise thin film deposition technique known as ALD [22] has been applied in the fabrication of MCP-PMTs to solve the lifetime issues [20]. Lin Chen et al. [8] indicated that using high SEY materials such as  $\text{Al}_2\text{O}_3$  and  $\text{MgO}$  as ALD coating materials on the upper surface of MCP can enhance the probability of collecting secondary electrons to improve CE to nearly 100% rather than being constrained by the MCP open area fraction. This enhancement allows for increased gain, improved single electron resolution, and a higher peak-to-valley ratio of MCP-PMTs [12].

In the performance tests to evaluate MCP-PMT by JNE, large charges are found in the SER charge spectrum of MCP-PMTs [36], as shown in the red histogram in Fig 1. Similar significant charges have also been observed in the mass testing of PMTs in JUNO, identified as the "long tail" in the SER charge distribution [1]. H. Q. Zhang et al. [37] used the SER charge model in Eq. (1) for large charges in JUNO and recommended the calibration of gain. A voltage division experiment reveals that the charge gain obtained from incident low-energy electrons is significantly smaller than that obtained from high-energy electrons, as measured by Yuzhen Yang et al. [35]. Thus, the gains of the secondaries are different from the photoelectrons entering the channels directly. The SER charge model in Eq. (1) is no longer sufficient to calibrate this type of PMT accurately. A mechanism is necessary to explain the formation of these significant charges and can thus develop an appropriate SER charge model for the MCP-PMT calibration.

In this paper, Gamma distribution is introduced in Sec. 2. In Sec. 3, a voltage-divided experiment is designed to measure the relationship between the gains of MCP and the energies of incident electrons. Considering the SEE model, we explain the cause of the large charges, and measure the total SEY of  $\text{Al}_2\text{O}_3$  and  $\text{MgO}$  for the incident 650 eV electrons. Based on the explanation, a Gamma-Tweedie mixture is proposed for MCP-PMT in Sec. 4. Discussion and conclusion are in Sec. 5 and Sec. 6.

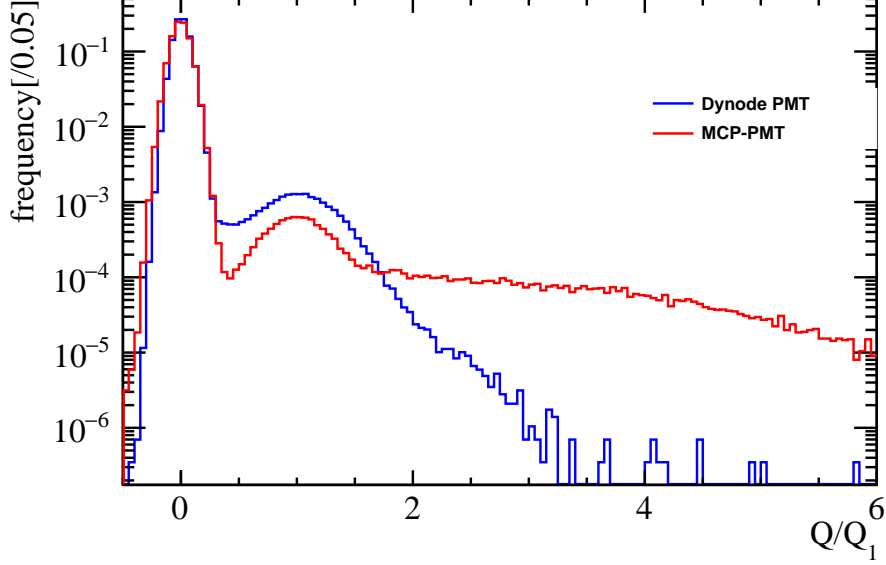


Figure 1: The SER charge spectra of MCP-PMT PM2112-9089F (red) and Dynode PMT (blue). The blue histogram consists of the pedestal and the peak of  $Q = Q_1$ , while the red histogram includes additional large charges.

## 2. SER charge spectrum based on Gamma distribution

Instead of Gaussian containing a small nonphysical tail less than 0, the charge distribution is parameterized with a Gamma distribution  $\Gamma(\alpha, \beta)$  defined by a scale factor  $\alpha$  and the rate factor  $\beta$  as Eq. (2):

$$f_{\Gamma}(x; \alpha, \beta) = \frac{x^{\alpha-1} e^{-\beta x} \beta^{\alpha}}{\Gamma(\alpha)} \quad \text{for } x > 0 \quad \alpha, \beta > 0 \quad (2)$$

where  $\Gamma(\alpha)$  is the Gamma function. A Gamma distribution uniquely determined by its expectation  $\frac{\alpha}{\beta}$  and variance  $\frac{\alpha}{\beta^2}$  which can be converted into the mean and the variance of the Gaussian.

Every multiplication of electrons at the dynodes or MCP channels follows a Poisson distribution [30]. A series of such multiplications forms a cascade Poisson distribution [4]. It is a Galton-Watson branching process [2] and difficult to perform analytical computations. Breitenberger summarized and indicated that the shape of SER charge spectrum is between the Poisson distribution and the Gaussian distribution [4]. Prescott proposed to utilize a cascade Polya distribution to characterize the electron multiplication in PMT when considering the non-uniformity of the dynode surface [28]. Kalousis approximated the Polya distribution as a Gamma distribution to calibrate PMT and achieved better calibration results than Gaussian model in Eq. (1) [15, 16]. Similar to Eq. (1), the SER charge spectrum based on the Gamma distribution is,

$$f(Q) = P_{\pi}(n_{\text{PE}}; \lambda) \otimes f_{\Gamma}(Q; n_{\text{PE}}\alpha, \beta) \quad (3)$$

80 where  $\frac{\alpha}{\beta} = Q_1$  and  $\frac{\alpha}{\beta^2} = \sigma_1^2$ .

### 81 3. Explanation for large charges based on secondary electron emission

#### 82 3.1. The structure of MCP-PMT

83 MCP-PMT deploys two pieces of MCPs as the electron multiplier. The photoelectrons are  
 84 amplified by MCP through a branching process described in Sec. 2 and a large number of electrons  
 85 produced at the end of the MCP reach the anode to form electrical signals [19].

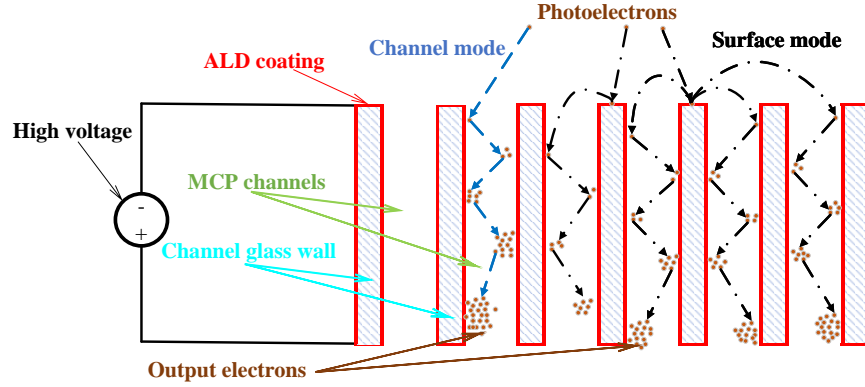


Figure 2: The photoelectrons directly enter the channels (channel mode) or hit the upper surface producing secondary electrons which enter the channels later (surface mode) [8]. After entering the MCP channel, the electron collides with the channel wall for many times and is amplified in a series of such multiplications [4].

86 Besides, the secondary electrons from the upper surface of MCP can also enter the MCP  
 87 channels for multiplication under the influence of electric field. Two independent mode dominate  
 88 the amplification process as shown in Fig. 2. The *channel mode* is that photoelectrons directly enter  
 89 the channels and the other is the *surface mode* that secondary electrons from the upper surface  
 90 enter the channels. The selection of these two modes follows Bernoulli distribution [4].

#### 91 3.2. Furman probabilistic model

92 The Furman probabilistic model (Furman model) [10] is a theoretical framework employed to  
 93 elucidate the phenomenon of SEE from solid surfaces. This model incorporates the statistical nature  
 94 of the SEE process by considering the probability distribution governing the number of secondary  
 95 electrons emitted per incident primary electron. Each emission event of a secondary electron is  
 96 regarded as an independent occurrence, with its energy following the distribution contingent upon  
 97 material properties and the primary energy.

98 In Furman model, the SES can be represented as  $d\delta/dE$ , where  $E$  is the energy of secondary  
 99 electron. There are three kinds of secondary electrons emitted. The first kind is the back-scattered  
 100 electron that secondary electrons are emitted by elastic scattering on the surface of the target  
 101 material. The SES is defined as Eq. (4), where  $\delta_{bs}$  is the yield of back-scatter electron,  $\theta(E)$  function  
 102 ensures the  $E < E_0$ ,  $E_0$  is the incident energy of the primary electron,  $\theta_0$  is the incident angle, and  
 103  $\sigma_{bs}$  is an adjustable standard deviation.

$$\frac{\delta_{bs}}{dE} = \theta(E)\theta(E_0 - E)\delta_{bs}(E_0, \theta_0) \frac{2 \exp(-(E - E_0)^2 / 2\sigma_{bs}^2)}{\sqrt{2\pi}\sigma_{bs} \operatorname{erf}(E_0/\sqrt{2}\sigma_{bs})} \quad (4)$$

104 The second kind is the rediffused electron that secondary electrons are generated by atomic  
 105 scattering after electrons enter the target material. The SES of rediffused electrons is defined as  
 106 Eq. (5), where  $\delta_{rd}$  the yield of rediffused electron, and  $q$  is an adjustable parameter.

$$\frac{\delta_{rd}}{dE} = \theta(E)\theta(E_0 - E)\delta_{rd}(E_0, \theta_0) \frac{(q + 1)E^q}{E_0^{q+1}} \quad (5)$$

107 The final and most important kind is the true-secondary electrons. Upon penetration of electrons  
 108 into the target material more deeply, intricate physical processes ensue, resulting in the generation of  
 109 one or more secondary electrons. This is the only one process which occurs with the multiplication  
 110 of electrons. The SES of true-secondary electrons is defined as Eq. (6).

$$\frac{d\delta_{ts}}{dE} = \sum_{n=1}^{\infty} \frac{n P_{n,ts}(E_0) (E/\epsilon_n)^{p_n-1} e^{-E/\epsilon_n}}{\epsilon_n \Gamma(p_n) P(np_n, E_0/\epsilon_n)} \times P[(n-1)p_n, (E_0 - E)/\epsilon_n] \quad (6)$$

111 where  $\delta_{ts}$  is the yield of true-secondary electrons,  $\epsilon_n$  and  $p_n$  are greater than 0 as phenomenological  
 112 parameters, and  $P(z, x)$  is the normalized incomplete gamma function satisfying  $P(0, x) = 1$ . The  
 113 number of true-secondary electrons is  $n$  following Poisson distribution  $n \sim \pi(\delta_{ts})$ ,  $P_{n,ts}$  is the  
 114 probability for emitting  $n$  true-secondary electrons defined in Eq. (7) [10].

$$P_{n,ts} = P(n; \delta_{ts}) = \frac{\delta_{ts}^n}{n!} e^{-\delta_{ts}} \quad (7)$$

115 The following parameters are taken as  $\delta_{bs} = 0.1$ ,  $\delta_{rd} = 1$ ,  $\delta_{ts} = 5$  [12],  $\theta_0 = 0$  and  $E_0 = 650$  eV,  
 116 and the total SES is  $f_{SES}(E) = \frac{d\delta}{dE} = \frac{\delta_{bs}}{dE} + \frac{\delta_{rd}}{dE} + \frac{\delta_{ts}}{dE}$  as shown in Fig. 3.

### 117 3.3. Voltage-division Experiment

118 From Sec. 3.2 and as shown in Fig. 3, secondary electrons have lower energies and usually less  
 119 than 100 eV when incident energy is 650 eV. When the primary energy is below 100 eV, the SEY is  
 120 much smaller than which at 650 eV [22]. Thus, the gain of single secondary electron is not the same

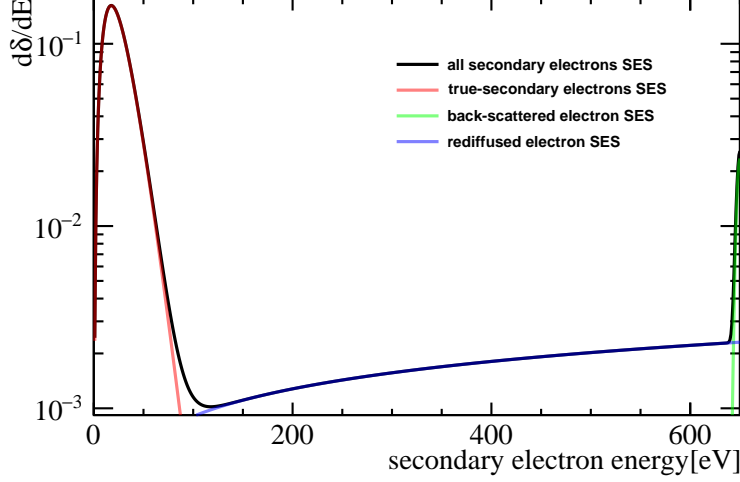


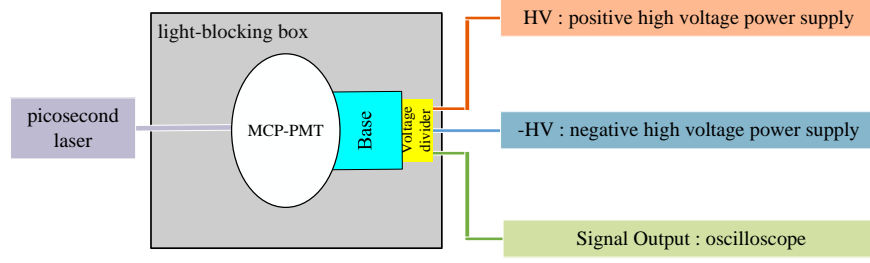
Figure 3: When primary energy is 650 eV, the red line represents  $d\delta_{bs}/dE$ , the blue line represents  $d\delta_{rd}/dE$ , the green line represents  $d\delta_{ts}/dE$ , and the black one is  $d\delta/dE$ .

as the photoelectrons directly entering the channels. A voltage-division experiment is designed to measure the relationship between the gains of MCP and the energies of electrons entering the MCP channels.

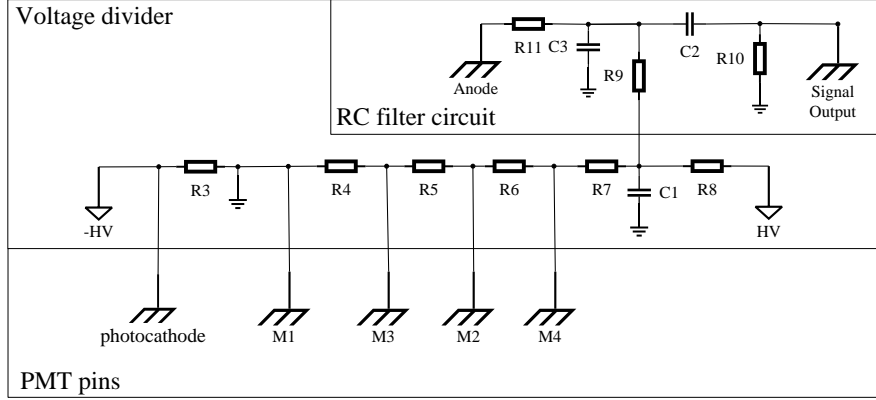
### 3.3.1. Experimental setup

The energy of the photoelectron arriving at the MCP is almost determined by the voltage difference between the photocathode and the MCP, based on which we can control the energy of the electrons by adjusting the voltage. As shown in the Fig. 4a, a positive and a negative high voltage supplies are used. A high sampling rate oscilloscope is used to capture all the waveforms.

As shown in Fig. 4b, an adjustable high voltage between the photocathode and M1 the upper surface of the first MCP is provided by the negative high voltage power supply. The positive high voltage power supply delivers 4 consistent voltages to the two MCPs after being divided by resistors as shown in Fig. 4a following the voltage divider designed in [21]. There is a stable voltage difference between the two MCPs defined as the gap voltage [35]. With this experimental setup, simultaneously adjusting the electron incident energy and keeping the voltage division of the MCPs stability are achieved. This can also be accomplished by using more power supplies [35] which is harder to operate but easier to change the voltage differences of MCPs.



(a)



(b)

Figure 4: Experimental setup and the circuit of voltage divider. The plot a is schematic diagram of the experimental setup: simultaneously supply positive and negative high voltages to the MCP-PMT, and capture the output waveforms using an oscilloscope. The plot b is the experimental circuit diagram: supply the photocathode with the negative high voltage, supply the two MCPs with the positive high voltage, and use an RC filtering and shaping circuit to convert the amplified electrical signal into waveforms output. M1, M3 are the upper surfaces of MCPs and M2, M4 are the lower surfaces. The gap voltage is between M2 and M3.

### 3.3.2. Relationship of gain and incident energy

A new waveform analysis method named fast stochastic matching pursuit (FSMP) [34] utilizing Markov Chain Monte Carlo is employed. With the best accurate time and intensity resolution, FSMP provides more precise measurements of SER charge spectrum.

To exclude the influence of the surface mode, we conducted the same test on MCP-PMTs with and without ALD coating. The  $\mu$  and  $\sigma$  are calculated for every initial energy by fitting the main peak of SER charge spectra with Gaussian distribution as shown in Fig. 5,  $g_{\mu,\sigma}(E)$  is the function to describe the relationship between gains and electron energies as shown in Fig. 6.

When the electron energy is less than 400 eV, the gain rapidly increases with the electron



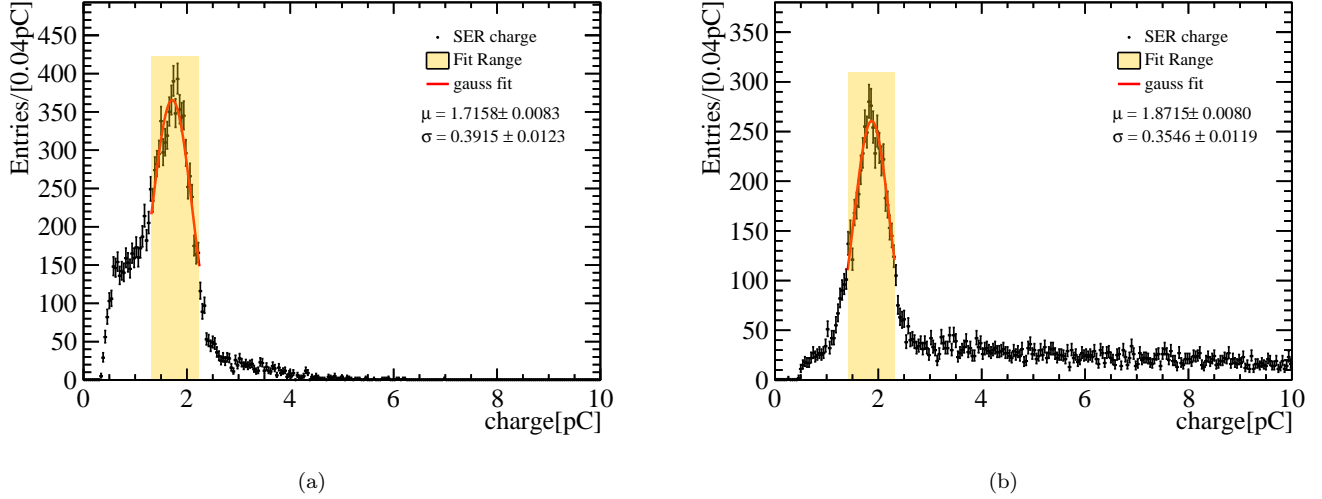


Figure 5: The plot [a](#) displays the fit of the charge spectrum of the MCP-PMT without ALD coating, while the plot [b](#) shows the fit with ALD coating. We observed that the plot [a](#) does not exhibit large charges.

energy. As the electron energy reaches 400 eV, the gain gradually stabilizes. Similar results are reported in [\[35\]](#). The gains for the low-energy secondary electrons from the surface mode are lower than that from channel mode.

The charge responses of electrons with different energies are superimposed according to the SES to obtain the charge response of the surface mode.

### 3.4. Monte Carlo calculation

Note the probability of electrons directly entering the channel and hitting on the MCP upper surface as  $p$  and  $1 - p$ . Considering that the number of secondary electrons  $n_{se}$  may exceed 1, The SER charge can be described as Eq. [\(8\)](#),

$$\begin{aligned}
 Q_{\text{MCP-PMT}} &= p \times Q_{\text{channel}} + (1 - p) \times Q_{\text{surface}} \\
 &= p \times Q_{\text{channel}} + (1 - p) \times \frac{\int_0^{E_0} G(E) f_{\text{SES}}(E) dE}{\int_0^{E_0} f_{\text{SES}}(E) dE}
 \end{aligned} \tag{8}$$

where  $Q_{\text{MCP-PMT}}$  is the SER charge distribution of MCP-PMT,  $Q_{\text{channel}}$  and  $Q_{\text{surface}}$  are the charge distributions of the charge mode and the surface mode, and  $G(E)$  whose parameters are taken from  $g_{\mu, \sigma}$  is the charge distribution when incident energy is  $E$ . The SER charge distribution is simulated using Monte Carlo method [\[25\]](#) as shown in Fig. [7](#). The probabilities of the three processes are approximated by the relative amounts of the yields. For true-secondary electrons, their number  $n$  is given by Poisson sampling and the sum of the sampled  $n$  charges serves as the output charge. Through the procedure, the charge response generated by a single electron incoming and by  $n_{\text{PE}}$

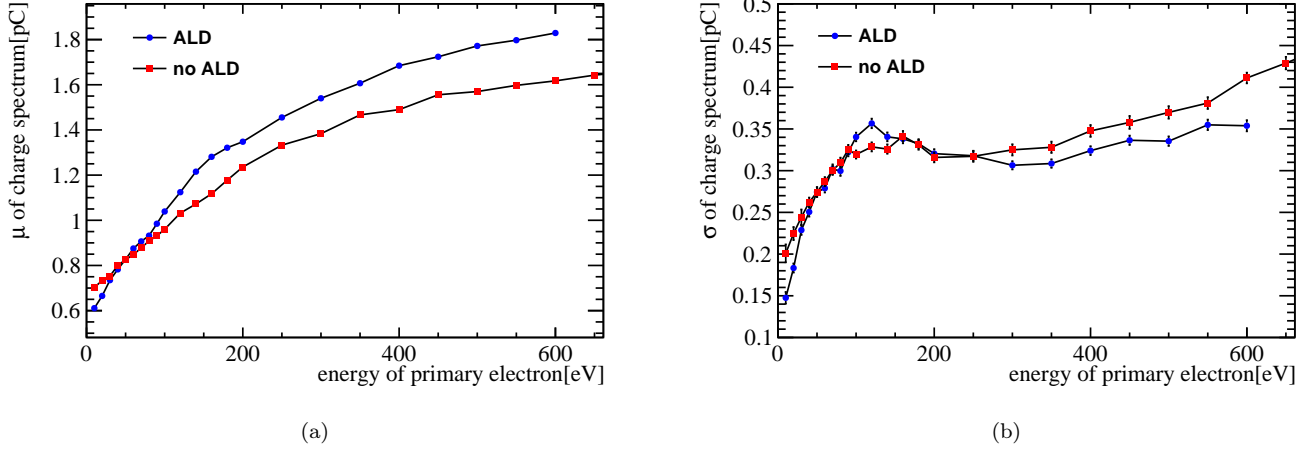


Figure 6: The plot [a](#) shows that the mean increases as initial electron energy increases, and the plot [b](#) shows the variance changes with energy. MCP-PMT with ALD coating (the red line) shows a similar variation trend to the one without ALD coating (the blue line).

are calculated. The charge distribution of the surface mode can be divided into three components according to the Furman model, the back-scattered electron mode defined as  $Q_{bs}$ , the rediffused electron mode defined as  $Q_{rd}$ , and the true-secondary electrons mode defined as  $Q_{ts}$ .

$$Q_{\text{surface}} = Q_{ts} + Q_{rd} + Q_{bs} \quad (9)$$

The back-scattered electron mode is predominantly distributed at the main peak, while the rediffused electron mode exhibits a distribution in close proximity to the main peak. These two components within the surface mode contribute to a single secondary emission electron. There exists little difference in energy between in the channel mode and in the back-scattered electron mode resulting in that the amplified charge is basically the same. Due to the energy of the rediffused electron slightly lower than that in the channel mode, the amplified charge after MCP multiplication is slightly smaller. Therefore, the contribution of these two modes to the large charges in SER charge spectrum can be considered negligible.

In the true-secondary electrons mode, the charge can be described as Eq. [\(10\)](#):

$$\begin{aligned} Q_{ts} &= \sum_{n=0}^{\infty} \sum_{i=0}^n Q_i \\ Q_i &\sim \Gamma(\alpha_i, \beta_i) \\ n &\sim \pi(\delta_{ts}) \end{aligned} \quad (10)$$

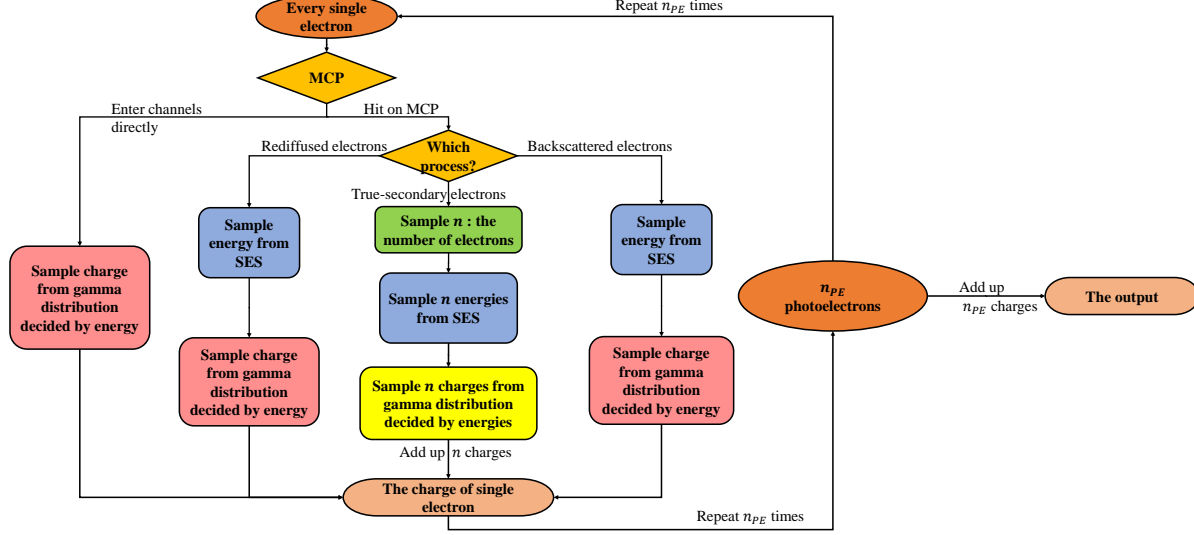


Figure 7: The procedure of Monte Carlo method for computing the SER charge spectrum.

175 The charge spectrum of different  $n$  is shown in Fig. 9. For each photoelectron in true-secondary  
 176 electrons mode, the output is the sum of the  $n$  charges and the bigger  $n$  is, the larger the charge is.  
 177 Due to the lower energy of the generated electrons, the charge after each electron multiplication is  
 178 smaller. It is challenging to distinguish the multiplied charges formed at the anode, as multiple  
 179 secondary electrons are generated and enter the MCP channels simultaneously. Their combined form  
 180 results in a larger charge formation, contributing to the "long-tail" of the SER charge spectrum.

### 181 3.5. Tuning model with experiment data

182 The field  $\delta_{ts}$  of the true-secondary electrons and the probability  $p$  in Eq. (8) which have a  
 183 significant impact on the SER charge distribution as shown in Fig. 10 are selected to generate  
 184 different histograms by MC.

185 A chi-square test is then performed between each MC histogram and the histogram of single  
 186 photoelectron charge obtained from the MCP-PMT test. The histograms of MC and test have  
 187 the same binning with the number of bins being  $r$ . The entries in  $i$ -th bin are  $n_i$  and  $m_i$ ; total  
 188 entries are  $N = \sum_{i=1}^r n_i$  and  $M = \sum_{i=1}^r m_i$ . The chi-square test indicates the similarity between  
 189 two histograms, with chi-square defined in Eq. (11) [11]. The chi-squares between the histograms  
 190 of MC and experiment data are scanned in the  $p - \delta_{ts}$  grid as shown in Fig. 11a. The distribution  
 191 of the chi-square with respect to  $p$  and  $\delta_{ts}$  is continuous, and a linear regression can be used to  
 192 fit the relationship between chi-square and  $p$  and  $\delta_{ts}$  [26]. For each MCP-PMT, the parameters

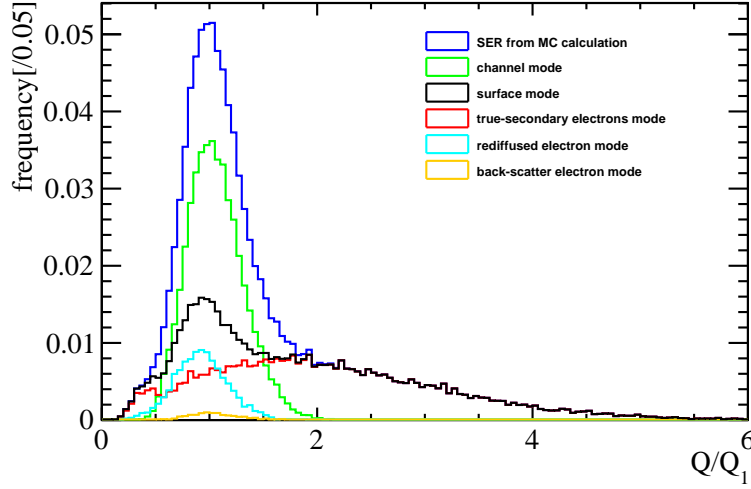


Figure 8: The charge distribution formed in the channel mode is concentrated around the main peak, while the tail portion is mainly generated by the true-secondary electrons in the surface mode.

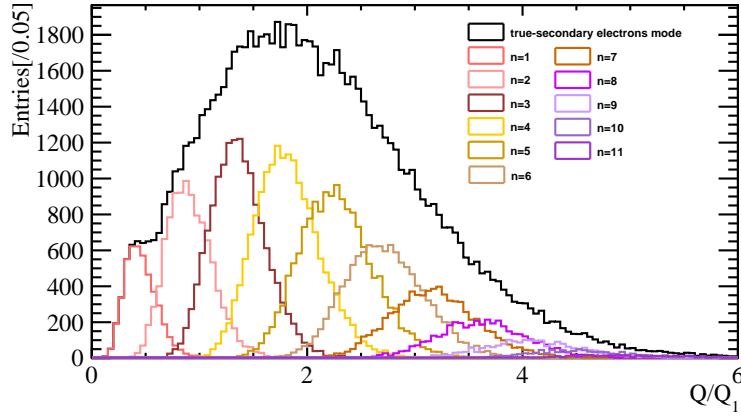


Figure 9: The charge distribution of true-secondary electrons mode in MC calculation when  $\delta_{ts} = 4.5$  and  $p = 0.5$ . The black histogram is the total distribution consisting of the histograms for different  $n$ .

193 corresponding to the minimum chi-square value are selected as the result. The confidence interval  
 194 for the parameters can be determined accordingly with a confidence level of 68.3% [9].

$$\chi^2_{(r-1)} = \sum_{i=1}^r \frac{(n_i - N\hat{k}_i)^2}{N\hat{k}_i} + \sum_{i=1}^r \frac{(m_i - M\hat{k}_i)^2}{M\hat{k}_i} = \frac{1}{MN} \sum_{i=1}^r \frac{(Mn_i - Nm_i)^2}{n_i + m_i} \quad (11)$$

$$\hat{k}_i = \frac{n_i + m_i}{N + M}$$

195 The scatter plot of the  $\delta_{ts}$  and  $p$  of 9 MCP-PMTs at the minimum chi-square is shown in Fig. 12.  
 196 The mean of  $\delta_{ts}$  is 5.98 and of  $p$  is 0.531, which means that on average, 0.531 electrons directly enter  
 197 the channel of the MCP. For each electron incident on the surface of the MCP, 5.98 true-secondary  
 198 electrons are multiplied.

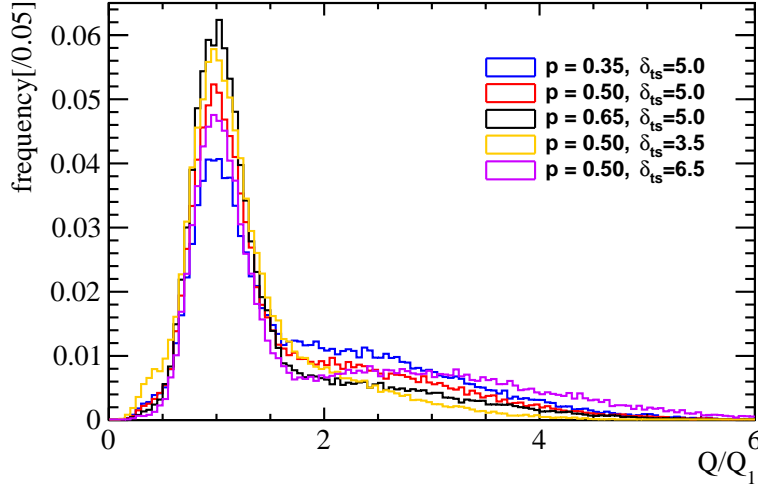


Figure 10: The shape of SER charge spectrum from MC is influenced by  $\delta_{ts}$  and  $p$ . As  $\delta_{ts}$  increases gradually, the height of the main peak region the tail gradually becomes longer and bigger. As  $p$  gradually increases, the height of the main peak region increases, and the tail gradually becomes narrower

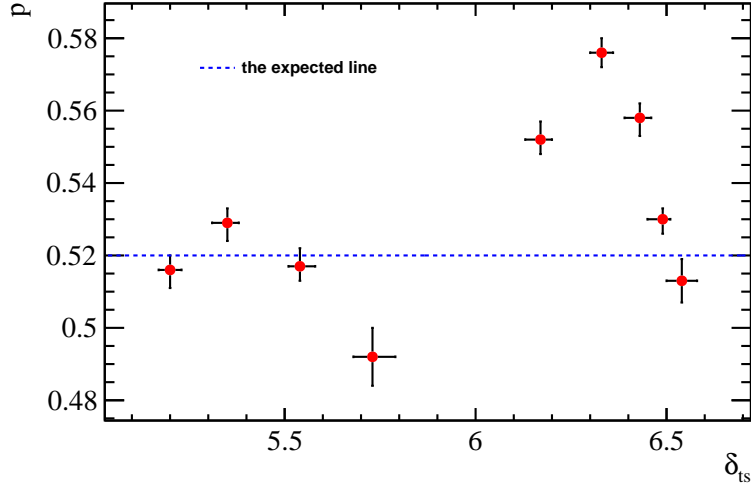


Figure 12: When convolving with 9 MCP-PMTs, the distribution of  $\delta_{ts}$  and  $p$  at the minimum chi-square occurs. The blue dashed line shows the expected  $p$ .

199 The MCP open area fraction of the MCP-PMT used in JNE is around 65% which is significantly  
200 higher than the result of the chi-squared test. Lin Chen. pointed out that there is the electrostatic  
201 lens effect at the MCP channel entrances reasulting in the ratio of photoelectrons entering MCP  
202 channels being smaller than the open area fraction. When photoelectrons come from the top of the  
203 MCP-PMT, the proportion of the photoelectrons directly entering the MCP channels is around  
204 60% while MCP open area fraction is 74.9% [8]. This ratio is extended to the MCP-PMT used  
205 in JNE, the stronger electric field brought by smaller PMT size is considered, and the open area

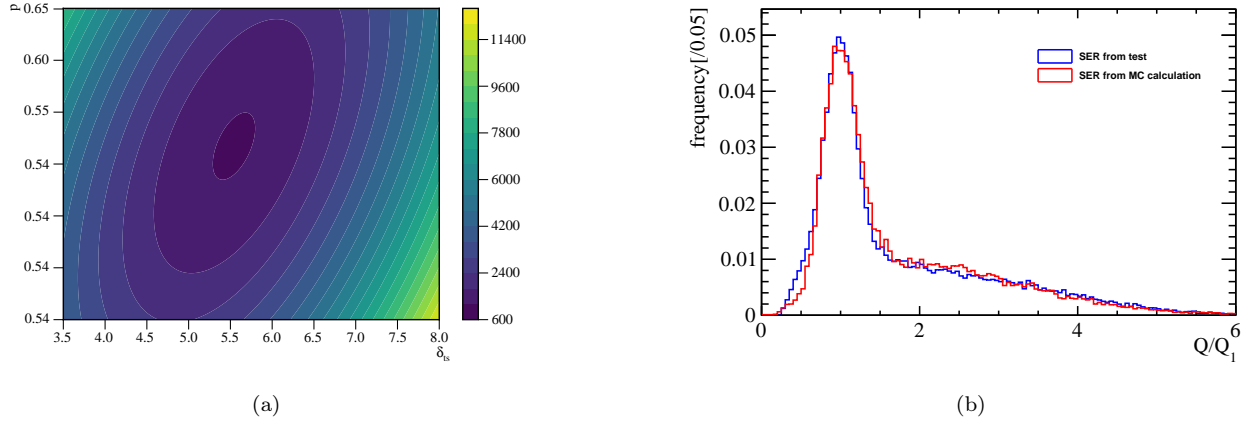


Figure 11: The plot [a](#) is the contour plot of the chi-square test, with  $p$  and  $\delta_{ts}$  as parameters and the chi-square values as the height. The plot [b](#) is an example of the MC histogram (the red line) and the histogram from test (the blue line).

fraction is smaller,  $52\% \pm 8\%$  is acceptable and the result of chi-square test is reasonable.

#### 4. Statistical model of SER for MCP-PMT

The MC calculation in Sec. 3.4 can be expressed using mathematical equations and abstracted into a model describing the charge of the MCP-PMT shown as Eq. (12):

$$\begin{aligned}
 Q_{\text{MCP-PMT}} &= p \times Q_{\text{channel}} + (1 - p) \times Q_{\text{surface}} \\
 &= p \times Q_{\text{channel}} + (1 - p) \times (p_{ts} \times Q_{ts} + p_{rd} \times Q_{rd} + p_{bs} \times Q_{bs}) \\
 &= p_0 \times Q_{\text{peak}} + (1 - p_0) Q_{ts} \\
 &= p_0 \times Q_{\text{peak}} + (1 - p_0) \sum_{n=0}^{\infty} \sum_{i=0}^n Q_i
 \end{aligned} \tag{12}$$

In Eq. (12), the spectra of  $Q_{\text{channel}}$ ,  $Q_{rd}$  and  $Q_{bs}$  are similar and merged into a new component defined as  $Q_{\text{peak}}$  which follows Gamma distribution. The other component is just  $Q_{ts}$  which is the reason for the generation of the large charges in SER charge spectrum.

In MC calculation,  $Q_i$  follows Gamma distribution  $\Gamma(\alpha_i, \beta_i)$  determined by  $E_i$ , the energy of true-secondary electrons which satisfies  $\sum_i^n E_i < E_0$ . Due to  $n$  following the Poisson distribution with a mean between 5 and 7, the probability of  $n$  exceeding 10 is negligible. At the same time, the total energy of the electrons is 650, which is tens of times the energy of the true-secondary electrons in the SES. The effect of  $n$  on  $E_i$  can be ignored and all the energies of true-secondary electrons follow the same distribution. As a result, the charge response of every true-secondary electron can

219 be treated indistinguishable regardless of the value of  $n$  shown in Fig. 13a. A Gamma distribution is  
 220 deployed to fit the charge response of single true-secondary electron shown in Fig. 13b and obtains  
 221 a sufficiently good fit.

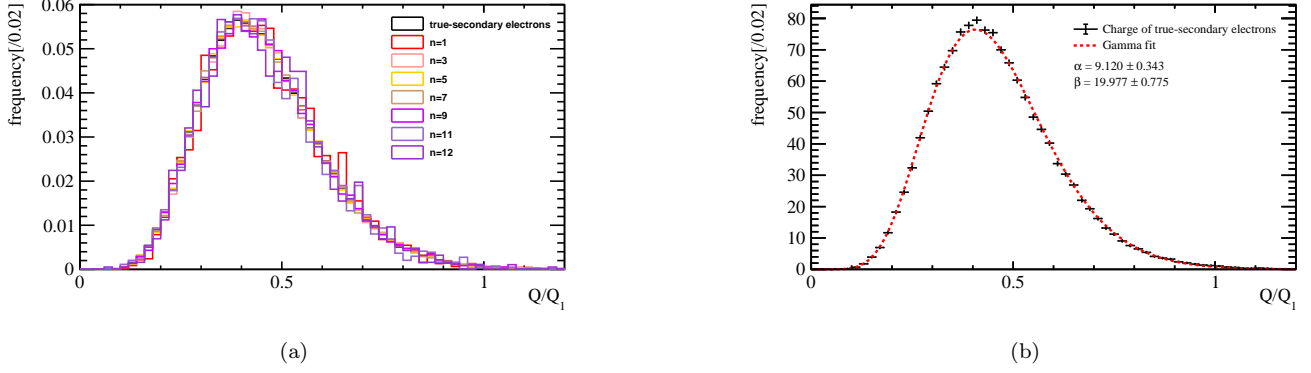


Figure 13: The charge response distribution of single true-secondary electron when  $n$  is different. The plot **a** shows that all the charges of true-secondary electrons follow the same distribution although  $n$  is different. The plot **b** shows that the fitting of Gamma distribution on the charge response of single true-secondary electrons achieves sufficient goodness.

222  $Q_{ts}$  can be written as a sum of the same  $n$  Gamma distributions as Eq.(13),

$$\begin{aligned}
 Q_{ts} &= \sum_{n=0}^{\infty} \sum_{i=0}^n Q_i \\
 Q_i &\sim \Gamma(\alpha, \beta) \\
 n &\sim \pi(\delta_{ts})
 \end{aligned} \tag{13}$$

223 which is a compound Poisson-Gamma distribution, belong to the Tweedie distribution ( $\text{Tw}_t(\alpha, \beta)$ )  
 224 when Tweedie power parameter  $t$  satisfies  $1 < t < 2$  [29, 14]. The SER charge spectrum can be  
 225 written as a Gamma-Tweedie mixture shown as Eq. (14):

$$\begin{aligned}
 Q_{\text{MCP-PMT}} &= p_0 \times Q_{\text{peak}} + (1 - p_0) Q_{ts} \\
 Q_{\text{peak}} &\sim \Gamma(\alpha_p, \beta_p) \\
 Q_{ts} &\sim \text{Tw}_t(\alpha, \beta), 1 < t < 2
 \end{aligned} \tag{14}$$

226 The MC calculation and chi-square test performed earlier in Sec. 3.4 and 3.5 essentially constitute  
 227 a joint fitting of the Gamma-Tweedie mixture. This type of fitting is rather complex and impractical,  
 228 requiring extensive computation.

## 229 5. Discussion

230 In experiments, it is also possible to consider incorporating the transit time distribution. In  
231 Sec. 3.4, compared to electrons directly entering the channels of the MCP, secondary electrons  
232 undergo a process of moving away from the MCP before being influenced by the electric field and  
233 returning to the MCP which increases the transit time. By using a testing system with extremely  
234 high time resolution, it may be possible to observe the three types of secondary electrons. The  
235 transit time distribution may exhibit a Gaussian peak caused by back-scattered secondary electrons  
236 after the main peak, while rediffused secondary electrons and true-secondary electrons contribute  
237 to a Gaussian peak near the main peak. Through fitting the charge spectrum and analyzing the  
238 transit time distribution, it becomes possible to predict the yields of the three types of secondary  
239 emission more accurately. Certainly,  $\delta_{ts}$  in this study is actually the product of the real SEY and  
240 the collection efficiency of the MCP for secondary electrons, and can be understood as the effective  
241 true-secondary emission yield.

242 By the Monte Carlo simulation, we propose the use of the Gamma-Tweedie mixture to describe  
243 the SER charge spectrum of the MCP-PMT. While the model is designed for the MCP-PMT,  
244 it can be extended to the Dynode-PMT as well, with the proportion  $p_0$  being nearly 0 while  
245 considering only one photoelectron hitting the first dynode. The first dynode is regarded as the  
246 MCP upper surface, the other dynodes are collectively considered as the MCP channels. However,  
247 no photoelectron enters the "channels" directly. In the future, it is possible to develop calibration  
248 methods specifically for this type of MCP-PMT to fully utilize its performance.

## 249 6. Conclusion

250 ALD-coated MCP-PMTs have the higher CE, while cause the large charges in SER charge  
251 spectrum shown in Fig. 1. An explanation based on the Furman secondary emission model and a  
252 voltage-division experiment are proposed. Through innovative design utilizing a dual high-voltage  
253 circuit in voltage-division experiment, the measurement of the gain response of MCP to electrons  
254 with different energies is achieved. Photoelectrons hitting the upper surface of MCP generate  
255 multiple true-secondary electrons entering the channels, which is the reason for the large charges in  
256 the SER charge spectrum of MCP-PMT.

257 By using the Monte Carlo method, the calculation of the SER charge spectrum of MCP-PMT  
258 has been achieved. By performing the chi-square test, the yield of true-secondary electrons can



be predicted which is the first study on the phenomenon of SEE in pulse mode. After conducting the chi-square test on 9 PMTs, the predicted yield is around 5.98. Based on the explanation, a Gamma-Tweedie mixture which is a new model for the SER charge spectrum of MCP-PMT has been proposed.

## 7. Acknowledgments

Special thanks to North Night Vision Science & Technology (Nanjing) Research Institute Co. Ltd. (NNVT) for providing all the PMTs and the voltage dividers we need. Also, we would like to thank Yiqi Liu, Jiashen Tao, Chuang Xu, Xin Wang and others for their assistance in the experiment, as well as Yuyi Wang for help with data analysis. Their support and assistance have been crucial to this study. This work is supported in part by the National Natural Science Foundation of China (12127808), National key research and development program of China (Grant no. 2023YFC3107400), and the Key Laboratory of Particle & Radiation Imaging (Tsinghua University).

## References

- [1] Angel Abusleme, Thomas Adam, Shakeel Ahmad, Rizwan Ahmed, Sebastiano Aiello, Muhammad Akram, Abid Aleem, Tsagkarakis Alexandros, Fengpeng An, Qi An, et al. Mass testing and characterization of 20-inch PMTs for JUNO. *The European Physical Journal C*, 82(12):1168, 2022.
- [2] M. S. Bartlett and Theodore Edward Harris. *The Theory of Branching Processes*. Springer Berlin, 1963.
- [3] E.H. Bellamy, G. Bellettini, J. Budagov, F. Cervelli, I. Chirikov-Zorin, M. Incagli, D. Lucchesi, C. Pagliarone, S. Tokar, and F. Zetti. Absolute calibration and monitoring of a spectrometric channel using a photomultiplier. *Nuclear Instruments and Methods in Physics Research Section A: Accelerators, Spectrometers, Detectors and Associated*, 339(3):468–476, 1994.
- [4] Ernst Breitenberger. Scintillation spectrometer statistics. *Progress in nuclear physics*, 4:56–94, 1955.
- [5] H Bruining and JH De Boer. Secondary electron emission: Part I. Secondary electron emission of metals. *Physica*, 5(1):17–30, 1938.

- [6] Meng Cao, Na Zhang, Tian-Cun Hu, Fang Wang, and Wan-Zhao Cui. Secondary electron emission from rough metal surfaces: A multi-generation model. *Journal of Physics D: Applied Physics*, 48(5):055501, 2015.
- [7] Zhen Cao, M. J. Chen, H. C. Li, and Z. G. Yao. Upgrading Plan Towards Multi-messenger Observation with LHAASO. *EPJ Web of Conferences*, 2019.
- [8] Lin Chen, Jinshou Tian, Chunliang Liu, Yifang Wang, Tianchi Zhao, Hulin Liu, Yonglin Wei, Xiaofeng Sai, Ping Chen, Xing Wang, Yu Lu, Dandan Hui, Lehui Guo, Shulin Liu, Sen Qian, Jingkai Xia, Baojun Yan, Na Zhu, Jianning Sun, Shuguang Si, Dong Li, Xingchao Wang, Guorui Huang, and Ming Qi. Optimization of the electron collection efficiency of a large area MCP-PMT for the JUNO experiment. *Nuclear Instruments and Methods in Physics Research Section A: Accelerators, Spectrometers, Detectors and Associated Equipment*, 827:124–130, 2016.
- [9] Glen Cowan. *Statistical Data Analysis*. Oxford University Press, Oxford: New York, illustrated edition edition, 1997.
- [10] MA Furman and MTF Pivi. Probabilistic model for the simulation of secondary electron emission. *Physical review special topics-accelerators and beams*, 5(12):124404, 2002.
- [11] N. D Gagunashvili. Comparison of weighted and unweighted histograms. *Statistics*, pages 43–44, 2012.
- [12] Lehui Guo, Liwei Xin, Lili Li, Yongsheng Gou, Xiaofeng Sai, Shaohui Li, Hulin Liu, Xiangyan Xu, Baiyu Liu, Guilong Gao, et al. Effects of secondary electron emission yield properties on gain and timing performance of ALD-coated MCP. *Nuclear Instruments and Methods in Physics Research Section A: Accelerators, Spectrometers, Detectors and Associated Equipment*, 1005:165369, 2021.
- [13] Slade J. Jokela, Igor V. Veryovkin, Alexander V. Zinovev, Jeffrey W. Elam, Anil U. Mane, Qing Peng, and Z. Insepov. Secondary Electron Yield of Emissive Materials for Large-Area Micro-Channel Plate Detectors: Surface Composition and Film Thickness Dependencies. *Physics Procedia*, 37:740–747, 2012.
- [14] B. Jorgensen. *The Theory of Dispersion Models*. Taylor & Francis, 1997.

- [15] Leonidas Kalousis. *Calibration of the Double Chooz detector and cosmic background studies*. PhD thesis, University of Strasbourg, 2012.
- [16] LN Kalousis, JPAM De André, E Baussan, and M Dracos. A fast numerical method for photomultiplier tube calibration. *Journal of Instrumentation*, 15(03):P03023, 2020.
- [17] N. Kishimoto, M. Nagamine, K. Inami, Y. Enari, and T. Ohshima. Lifetime of MCP-PMT. *Nuclear Instruments and Methods in Physics Research Section A: Accelerators, Spectrometers, Detectors and Associated Equipment*, 564(1):204–211, 2006.
- [18] S. Krauss, M. Böhm, K. Gumbert, A. Lehmann, D. Miehl, A. Belias, R. Dzhygadlo, A. Gerhardt, D. Lehmann, K. Peters, G. Schepers, C. Schwarz, J. Schwiening, M. Traxler, Y. Wolf, L. Schmitt, M. Düren, A. Hayrapetyan, I. Köseglu, M. Schmidt, T. Wasem, C. Sfienti, and A. Ali. Performance of the most recent Microchannel-Plate PMTs for the PANDA DIRC detectors at FAIR. *Nuclear Instruments and Methods in Physics Research Section A: Accelerators, Spectrometers, Detectors and Associated*, 1057:168659, 2023.
- [19] Peter KriAn and Samo Korpar. Photodetectors in Particle Physics Experiments. *Annual Review of Nuclear & Particle Science*, 63(1):329–349, 2013.
- [20] A Lehmann, A Belias, R Dzhygadlo, A Gerhardt, D Lehmann, K Peters, G Schepers, C Schwarz, J Schwiening, M Traxler, et al. Latest Technological Advances with MCP-PMTs. 2374(1):012128, 2022.
- [21] Feng-Jiao Luo, Zhi-Min Wang, An-Bo Yang, Yue-Kun Heng, Zhong-Hua Qin, Mei-Hang Xu, Sen Qian, Shu-Lin Liu, Yi-Fang Wang, Wei Wang, et al. Design & Optimization of the HV divider for JUNO 20-inch PMT. *arXiv preprint arXiv:2307.10544*, 2023.
- [22] Anil U. Mane, Qing Peng, Jeffrey W. Elam, Daniel C. Bennis, Christopher A. Craven, Michael A. Detarando, John R. Escolás, Henry J. Frisch, Slade J. Jokela, and Jason Mcphate. An Atomic Layer Deposition Method to Fabricate Economical and Robust Large Area Microchannel Plates for Photodetectors. *Physics Procedia*, 37:722–732, 2012.
- [23] K. Matsuoka. Development and production of the MCP-PMT for the Belle II TOP counter. *Nuclear Instruments and Methods in Physics Research Section A: Accelerators, Spectrometers, Detectors and Associated Equipment*, 766:148–151, 2014.

- [24] R Nathan and CHB Mee. The energy distribution of photoelectrons from the K2CsSb photocathode. *physica status solidi (a)*, 2(1):67–72, 1970.
- [25] Von Neumann. Various techniques used in connection with random digits. *Notes by GE Forsythe*, pages 36–38, 1951.
- [26] Hyunseung Oh, Douglas C. Montgomery, Elizabeth A. Peck, and G. Geoffrey Vining. Introduction to Linear Regression Analysis. *Biometrics*, 69(4):1087–1087, 2013.
- [27] L. Olano and I. Montero. Energy spectra of secondary electrons in dielectric materials by charging analysis. *Results in Physics*, 19:103456, 2020.
- [28] JR Prescott. A statistical model for photomultiplier single-electron statistics. *Nuclear Instruments and Methods*, 39(1):173–179, 1966.
- [29] Ananda Sen. The Theory of Dispersion Models. *Technometrics*, 41:177–178, 1997.
- [30] Harry H Tan. A statistical model of the photomultiplier gain process with applications to optical pulse detection. 1982.
- [31] Y Ushio, T Banno, N Matuda, Y Saito, S Baba, and A Kinbara. Secondary electron emission studies on MgO films. *Thin Solid Films*, 167(1-2):299–308, 1988.
- [32] Q. Wu, S. Qian, Y. Cao, G. Huang, M. Jin, Z. Jin, D. Li, H. Liu, K. Li, S. Liu, L. Ma, L. Ren, S. Si, J. Sun, J. Tian, X. Wang, H. Zhan, Y. Zhu, and on behalf of the MCP-PMT workgroup. Summary of the R&D of 20-inch MCP-PMTs for neutrino detection. *Journal of Instrumentation*, 16(11):C11003, nov 2021.
- [33] J. Xia, S. Qian, W. Wang, Z. Ning, Y. Cheng, Z. Wang, X. Li, M. Qi, Y. Heng, S. Liu, and X. Lei. A performance evaluation system for photomultiplier tubes. *Journal of Instrumentation*, 10(03):P03023, Mar 2015.
- [34] D.C. Xu, B.D. Xu, E.J. Bao, Y.Y. Wu, A.Q. Zhang, Y.Y. Wang, G.L. Zhang, Y. Xu, Z.Y. Guo, J.H. Pei, H.Y. Mao, J.S. Liu, Z. Wang, and S.M. Chen. Towards the ultimate PMT waveform analysis for neutrino and dark matter experiments. *Journal of Instrumentation*, 17(06):P06040, jun 2022.

- [35] Yuzhen Yang, Baojun Yan, Shulin Liu, Tianchi Zhao, Yang Yu, Kaile Wen, Yumei Li, and Ming Qi. MCP performance improvement using alumina thin film. *Nuclear Instruments and Methods in Physics Research Section A: Accelerators, Spectrometers, Detectors and Associated Equipment*, 868:43–47, 2017.
- [36] Aiqiang Zhang, Benda Xu, Jun Weng, Huiyou Chen, Wenhui Shao, Tong Xu, Ling Ren, Sen Qian, Zhe Wang, and Shaomin Chen. Performance evaluation of the 8-inch MCP-PMT for Jinping Neutrino Experiment. *Nuclear Instruments and Methods in Physics Research Section A: Accelerators, Spectrometers, Detectors and Associated*, 1055:168506, 2023.
- [37] H.Q. Zhang, Z.M. Wang, F.J. Luo, A.B. Yang, D.R. Wu, Y.C. Li, Z.H. Qin, C.G. Yang, Y.K. Heng, Y.F. Wang, and H.S. Chen. Gain and charge response of 20" MCP and dynode PMTs. *Journal of Instrumentation*, 16(08):T08009, 2021.
- [38] Yao Zhu, Yiqi Cao, Feng Gao, Guorui Huang, Muchun Jin, Zhen Jin, Dong Li, Kun Li, Shulin Liu, Sen Qian, Ling Ren, Shuguang Si, Jianning Sun, Xingchao Wang, Zhile Wang, Fei Xie, and Haoda Zhang. The mass production and batch test result of 20" MCP-PMTs. *Nuclear Instruments and Methods in Physics Research Section A: Accelerators, Spectrometers, Detectors and Associated Equipment*, 952:162002, 2020. 10th International Workshop on Ring Imaging Cherenkov Detectors (RICH 2018).